UNIVERSITY
of York

SCHOOL OF PHYSICS, ENGINEERING, AND TECHNOLOGY

Stochastic Optimisation of Aperiodic Phased Array Designs with Beamforming Techniques in the SAMI-2 Diagnostic

Matthew Cox

BSc Project in Physics

Project Supervisor: Prof. Roddy Vann

May 2023

Abstract

This project sought to determine the optimal arrangement of antenna elements on a phased antenna array. A phased array is an antenna system composed of multiple individual antenna elements arranged in a specific pattern. The focus was in using programs to automatically arrange antennas, score the layout and then iteratively improve their positions. In order to approximate array performance, novel numerical methods were created by the author. The overarching contribution made in this report is an improved phased antenna array design that will be integrated into the Synthetic Aperture Microwave Imager 2 (SAMI-2), a diagnostic that uses microwaves to probe various plasma edge properties inside the spherical tokamak in the MAST facility in Culham, UK. With regards to the methods and outcomes of the array design, the author used stochastic optimisation in conjunction with beamforming techniques to iteratively improve the performance, on multiple metrics, of any given phased array. A variety of objective functions were tested as a proxy for the full beamformed derived performance. One such proxy objective function quantified the uniformity of the distribution of all antenna pair separations and angles; this showed promise in improving angular resolution, but to the detriment of sidelobe rejection. The array this paper proposes has 20 antenna elements, a predicted sidelobe rejection value of (-8.1 ± 0.2) dB, an angular resolution of $(5.4 \pm 0.1)°$ and a directivity of (13.4 ± 0.2) dB for microwaves at 20 GHz. The results of this study demonstrate the feasibility of using full beamforming calculations within an optimisation function when designing aperiodic arrays. As an addition to this project, images were reconstructed from virtual data using both the proposed array and the one currently in SAMI-2. However the validity of these images is greatly limited due to the assumption of idealised data.

Contents

1   Introduction

Before the invention of the phased antenna array (PAA), directing radiation required physically altering an antenna's orientation. Karl Ferdinand Brau's early 20th-century experiments led to the discovery of beamforming [1], enabling radio wave interference pattern manipulation through altering each antennas' phase and amplitude. This enabled electronic steering of antenna radiation patterns without physical movement, revolutionizing wireless communication and and laying the groundwork for the development of phased antenna arrays. Phased arrays have since found applications in a variety of sectors beyond their initial military and defence use. They are now utilised in telecommunications, radar and sonar systems, medical imaging, and radio astronomy among other areas [2][3][4].

Phased array technology is integral to the Synthetic Aperture Microwave Imager (SAMI-2), a microwave imaging diagnostic that occupies a port window in the MAST-U spherical tokamak in Culham, UK. The core motivation behind the SAMI-2 diagnostic is the need for rapid, high-quality data acquisition of plasma edge properties critical for monitoring stability. These properties can be probed actively or passively, meaning SAMI-2 can emit radiation and analyse reflections through Doppler Backscattering (DBS) or passively image the microwave radiation to detect spontaneous emissions. Doppler Backscattering uses the frequency shift between the emitted and received radiation to infer particle velocity. This data can then be used to inform plasma control mechanisms in the tokamak such as current drive experiments [5].

Consider incident EM radiation on two antennas, as seen in Figure 1. Given that these antennas are placed at different positions, the radiation travels further to reach one than the other, resulting in a time delay, and therefore, a phase delay. Converting phase delay to a path difference, multiple possible radiation directions can be theorised. Placing an additional antenna would add two more baselines, as these antenna-pair vectors are called, further restricting the space of all possible radiation directions. However, a new baseline identical to a previous one won't collect new phase information, leading to baseline redundancy.
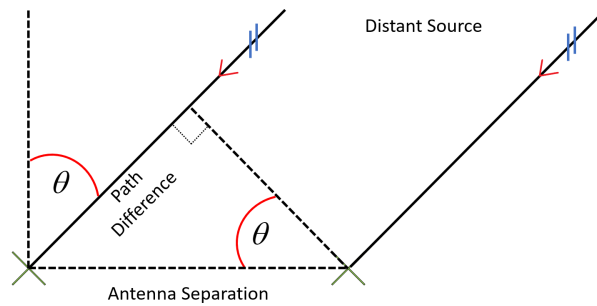

Figure 1: Diagram of two antennas with a distant radiation source defining antenna separation, source direction and path difference

From a measured phase difference between the two antennas in Figure 1, the possible path differences as annotated in the figure becomes:

$$\Delta x_n = \frac{\lambda}{2\pi}(\Delta\phi + n2\pi) \qquad (1)$$

where Δx_n is the path difference for a given n, $\Delta\phi$ is the measured phase difference, n is any real integer to account for phase differences greater than 2π and λ is the wavelength. The importance of eq. 1 is that the direction can be directly extracted when the antenna pair separation is known:

$$\theta_n = \arctan(\frac{\Delta x_n}{d}) \qquad (2)$$

where θ_n is defined for a given n in Figure 1 and d is the antenna pair separation.

The primary objective of this project was to develop a method of automating the design process of the front-panel antenna layout in SAMI-2. More specifically, the goal was to maximise the performance of the array by minimising the beam-width and sidelobe power. The beam-width in this report is the half-power beam-width (HPBW) and represents the size of the radiation pattern's main beam at a given distance. Sidelobes in phased arrays are directions of unwanted radiation outside the main beam. The secondary objective was to develop scripts for data analysis, image reconstruction, and troubleshooting of the array's experimentally collected data. These goals were achieved, in that the project produced an improved array, with 20 dual-polarisation sinuous antenna elements as opposed to the previous 9, that is on track to be implemented into SAMI-2 [6].

There are a number of different approaches others have taken to finding an optimal solution to this antenna layout problem, including genetic algorithms, particle swarms, and simulated annealing [7][8]. However, these methods are often used to create arrays with a certain degree of regularity, for example, clustered, thinned, or sparse arrays, whereas our problem demands an approach suitable for aperiodic array architectures. Aperiodic means there is no pattern present. Advanced techniques such as compressed sensing have been applied to irregular phased arrays, however, they were deemed beyond the reach of this project [9]. Consequently, a more straightforward yet effective algorithm was selected to tackle this particular design challenge: the stochastic optimization algorithm. The term "stochastic" refers to the random sampling of a specific parameter. In this context, it involves randomly and iteratively perturbing each antenna element in a direction that increases a pre-defined objective function. This approach has historically been avoided due to the high computational costs incurred in reaching an optimal solution. Nonetheless, in this project an efficient algorithm for calculating certain desirable quantities such as gain and beam-width was devised, allowing this approach to be feasible.

In terms of the latter aim of analysing data collected from SAMI-2, a horn antenna was positioned inside an anechoic chamber facing SAMI-2. Simple scripts were written in Python to process and visualise voltage data, as well as to analyse frequency spectra and coherence relationships for both mixers and antennas. This code aided in the identification of malfunctioning IQ mixers and antennas while allowing preliminary investigations into cross talk. Although carried out on an array identical to the array currently in SAMI-2, the same procedures apply to any other similar phased array such as the one put forward in this report. Multiple objective functions for the PAA optimizer

were evaluated, but the decided upon approach was to generate an interference pattern as generated by isotropically emitting antenna elements. The real component of the electric field at the antenna was assumed to be a plane wave governed by the following equation:

$$A(d, t) = \frac{1}{d} \cos(kd - \omega t) \tag{3}$$

where A is the amplitude, d is the distance from source to image pixel, k is the wave number, ω is angular frequency and t is time.

The precise methodology in generating the interference pattern using eq. 3 will be discussed later in the report. This pattern was crucial to scoring the array designs and relied on beamforming in its construction. Beamforming is the process by which specific phase shifts and amplitudes are introduced to each antenna such that the overall radiation pattern is focused and directed. When creating an image using a phased array, the beamforming process directs the array onto one location at a time, then measures the intensity of the signal from that location. However, with sidelobes present, although the array is pointed in one direction, it is now sensitive to signals originating from another. They often lead to undesirable image artefacts, so it is crucial to quantify this effect. The sidelobe rejection value is the relative power of these zones as compared to the mainlobe in the centre of the image. Throughout this report, the theory assumes each antenna element on SAMI-2 receives and emits evenly from all direction or isotropically. Therefore, the theoretical interference pattern assumes a spherical emission pattern as evident in the *1/d* attenuation coefficient in eq. 3.

2 Method

2.1 Design of The Phased Array

We seek a computationally efficient objective function by which to score our phased array design in the stochastic optimiser. A fitting scoring function might aim to increase the maximum image resolution of SAMI-2. One method of achieving this, is to maximise the number of points sampled in Fourier space. Each independent baseline, the vector between an antenna pair, in the array will capture a different spatial frequency, which is to say it will measure different spatial features in radiation. Therefore, more independent baselines leads to a higher resolution, also the larger these baselines the smaller the changes or features have to be in order for SAMI-2 to detect them. In other words, given a specific number of antennas, it is favourable to maximise both the distribution uniformity of antenna pair separations and their respective angular orientations to enhance resolution and detection capabilities. This report will briefly cover a couple objective functions and give justifications for the final choice. The author used Python for this project due to its ease of use in manipulating matrices and vectors using the NumPy library.

2.1.1 Beamforming Interference Pattern Generation

1. The separations between each antenna-pixel pair are calculated and stored in a matrix, D. Every antenna has a vector of all image pixels associated with it.

$$D_{ij} = \sqrt{(x_i - x_j)^2 + (y_i - y_j)^2 + (z_i - z_j)^2} \tag{4}$$

where (x_i, y_i, z_i) are the coordinates of the ith antenna element and (x_j, y_j, z_j) are the coordinates of the jth screen pixel.

2. Next, the expected instantaneous intensity for each pixel is calculated.

$$I_j(t) = \left(\sum_{i=1}^{N} \frac{1}{D_{ij}} \cos(kD_{ij} - \omega t) \right)^2 \tag{5}$$

where N is the number of antenna elements, k is the wave number, and ω is the angular frequency of the microwave radiation.

3. The time averaged intensity for a given element of the final image vector is then given by:

$$\bar{I}_j = \frac{1}{T} \int_0^T I_j(t) dt \tag{6}$$

where T is the time period of oscillation, and the integration is approximated by averaging over a fixed number of time steps. When calculating the mean intensity over this time period, the interference pattern converges to a constant image relatively quickly, and the additional benefit of using more than 3 time steps becomes negligible.

4. Finally, the interference pattern is generated by reshaping the intensity vector $\bar{I}_j$, into a two-dimensional image with *Image Resolution*, as defined in Table 1, as the number of pixels wide and high.

The position and resolution of the imaging screen, the width of the image, and the frequency of radiation all contribute to the final image. Consequently, they also influence any performance metrics derived from it. These parameters were chosen such that the final sidelobe rejection value and beam-width remain stable and do not change significantly as the parameter is changed further. The computational costs scale with the square of the resolution and so it is favourable to pick a small value. However, with too small a resolution the spatial fidelity becomes poor and properties such as beam-width fluctuate significantly. 100 pixels wide and 100 pixels high provided an image that allowed for reliable determination of gain and beam-width while remaining fast to compute. SAMI-2 operates at a frequency range of $(20 - 40)$ *GHz* and so a frequency of 20 *GHz* was chosen.

Parameter	Value (*mm*)
Image Resolution	10
Image Width	1000
Wavelength	15

Table 1: Table of Interference Pattern Parameters

6

2.1.2 Optimization Constraints in Antenna Layout

For the iterative improvement of a phased array antenna design, an environment with appropriate physical constraints must first be established, within which the antenna elements can manoeuvre without collisions or risk of boundary escape. In the case of SAMI-2, three crucial components must be taken into account as they constrain the cross-section of each antenna. Positioned perpendicularly behind each antenna, relative to the array's face, are: a printed circuit board (**PCB**), WithWave connectors (**WWCs**), and sub-miniature push-on connectors (**SMPs**). These components are represented by rectangles as demonstrated in Figure 2.
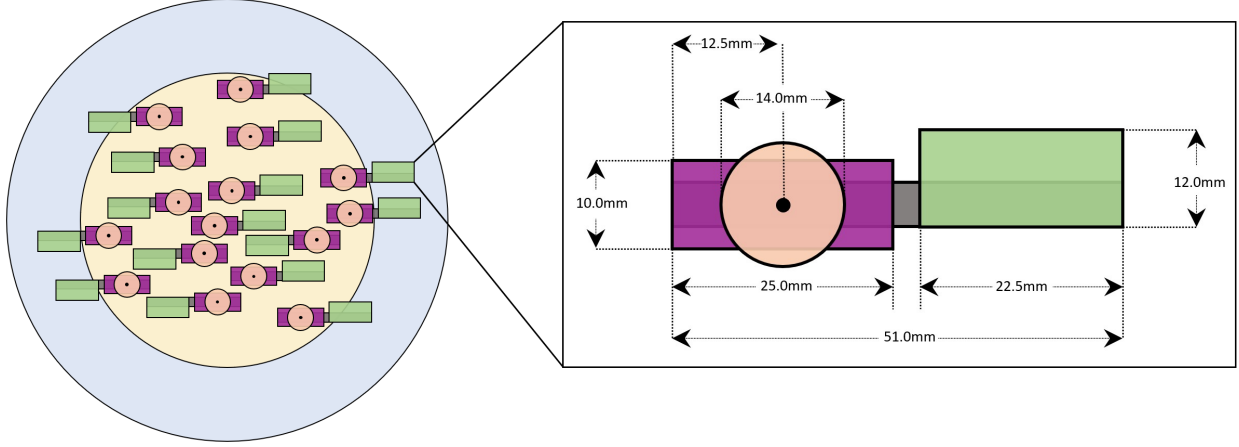

Figure 2: Example array design (*left*) and an annotated diagram (*right*) of the rectangles used to model the PCBs (*grey*), SMPs (*green*), WWCs (*purple*) and antennas (*orange*)

An example array design in Figure 2 shows the inner circle to constrain the antenna and an outer circle that constrains all other components. In the optimisation programs, an additional 5% tolerance was added to all values quoted in Figure 2. Several important constraints for the optimisation process are defined in Table 2

Parameter	Value (mm)
Outer Array Radius	120.0
Inner Array Radius	80.0
Perturbation Mean	0.0
Perturbation Standard Deviation	14.0

Table 2: Table of Antenna Design Parameters

2.1.3 Objective Function

Various objective functions were tested to quantise some crucial aspect of the phased arrays performance. Central beampower, beam-width, 2D local peak-searches and baseline redundancy minimisation were all trialled with varying degrees of success. The most promising approaches were initially those which tried to maximise the uniformity of the distribution of antenna pair separations

in x and y. The idea behind this is that the phased array collects its information using the relative phase differences between all antenna pairs; this means that if an antenna pair detects the same phase difference as another pair, it would be redundant. In other words, no two baselines should be the same.

However, when applied to the optimization program, the gain of the antenna array consistently decreased as the antennas were pushed out to the edges in an annular pattern. On the other hand, the beam-width did decrease as intended, but it came at the expense of a restricted field of view due to the port window lip. As a result of this decreased gain and restricted field of view, these methods were ultimately disregarded.

It was decided that in order to create the most accurate metric for performance, the interference pattern would be used directly. Initially, this was not feasible due to the speed of computation, however, after vectorising operations, it became suitable for use. The final objective function used a central circular overlay that encloses the mainlobe on the interference pattern and found the maximum power inside that circle compared to the maximum power outside. This ratio was used to approximate the sidelobe rejection values of the array. The diameter of this circle was chosen to be $0.2m$ at $1m$ or $\approx 11°$ because that value fully encloses, with a surrounding buffer region, the mainlobe.

The final objective function was chosen because of its ability to accurately approximate the sidelobe rejection value while maintaining computational speed and restricting the beam-width. This estimated sidelobe rejection value is given by:

$$\text{SLL}(I_j) = 10 \cdot \log \left(\frac{\max(I_j M_j)}{\max(I_j)} \right) \tag{7}$$

where $\text{SLL}(I_j)$ is the approximate sidelobe level of the phased array, M_j is an element of circular mask, $\mathbf{M}$, with the same dimensions as the interference pattern but with 0s for every pixel inside the cut-off region and 1s elsewhere and I_j is the interference pattern. When multiplied element-wise, this mask essentially cuts out a central circle from the image, thus, the maximum value outside the white circle is given by $\max(I_j M_j)$.
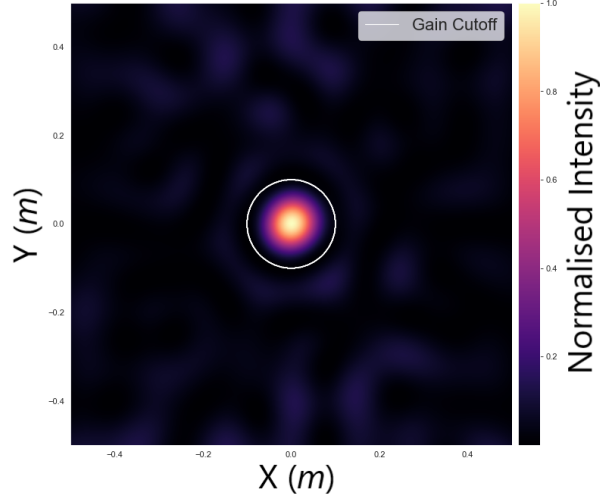
Figure 3: Interference pattern of the final 20-antenna array with the circular cut-off shown in white

To account for the non-ideal nature of the final physical array a small random adjustment is made to the final score, representing a possible error in the calculation. This allows the score to occasionally decrease, a concept similar to that of 'accepting a worse solution' with a certain decreasing probability in simulated annealing [12][14]. Therefore, the final objective function takes the form:

$$f(I_j) = -\text{SLL}(I_j) - U(a,b)\text{SLL}(I_j) \qquad (8)$$

where $f(I_j)$ is the objective function, U is a uniform distribution between bounds $a = -0.05$ and $b = 0.05$.

2.1.4 Optimisation Process

An initial, randomised array is constructed by systematically placing elements onto the array while adhering to the predefined boundaries and preventing collisions. This procedure is executed as described in the following flow chart.
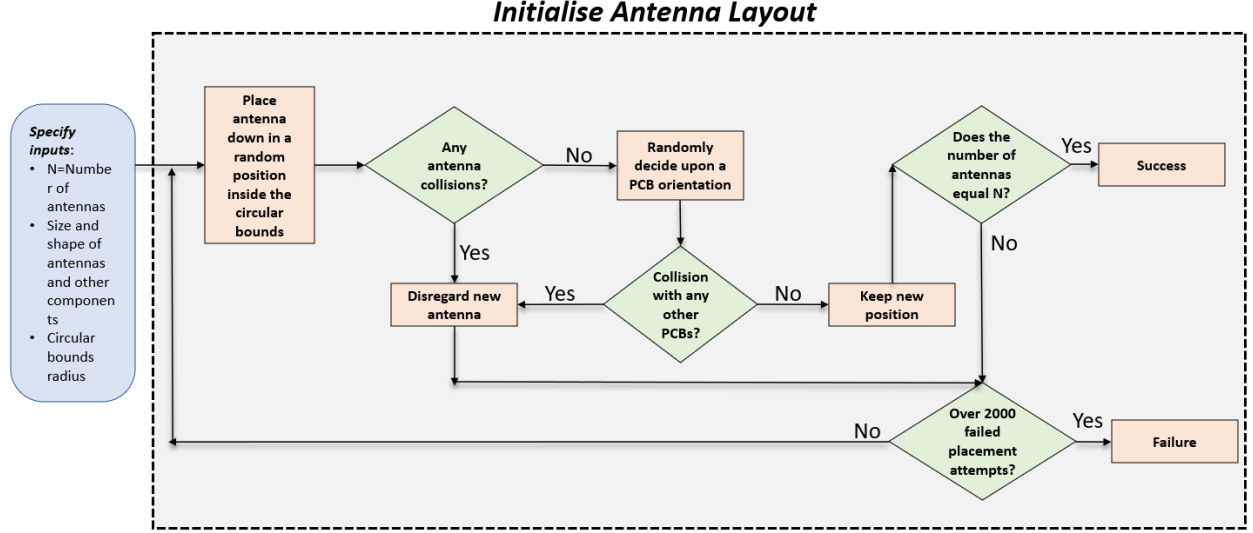
9

Figure 4: Flow chart of the initial array creation process

1. Each antenna is sequentially perturbed according to two random samples drawn from a normal distribution, which correspond to adjustments in the *x* and *y* directions. The utilisation of a normal distribution enables sporadic and larger leaps to evade potential local minima.

2. The score, *f* , is calculated for every antenna adjustment made, and the adjustment is only kept if the score increases. It should be noted that all PCBs were constrained to maintain a horizontal orientation, but they were allowed to flip if by doing so improved their score.

3. The above steps are repeated until the score has reached a steady state.

2.2 Array Performance Evaluation

2.2.1 Beam-Width Determination

In the analysis of phased antenna arrays, it is common practice to calculate the beam-width using the half-power beam-width (HPBW), which represents the point at which the signal power decreases to half, or -3 dB below its maximum power [13].

Although the HPBW calculations offer valuable insights into the predicted performance of phased array antennas, they were not incorporated into the previously mentioned objective function. Similar to the SLL calculations, there are no analytic solutions available for the determination of beam-width for 2D aperiodic arrays. As a result, a numerical approximation was made using line profiles through the interference pattern. Multiple line profiles, evenly rotated around the pixel of maximum brightness, were sampled from the interference pattern, as seen in Figure 5. By computing the average profile, the HPHM can then be calculated by determining the distance between the two points that are -3 dB down from the maximum intensity. This HPBW can then be used to quantify the angular resolution given that the image screen is 1m away.
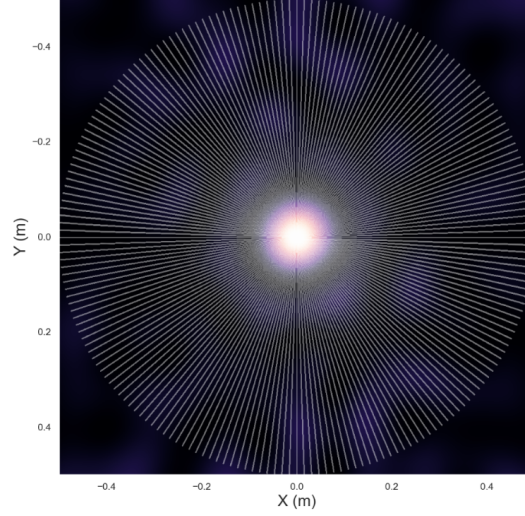
Figure 5: Visualisation of 100 line profiles taken through the 20-antenna interference pattern

To illustrate the HPBW procedure, see the following figure which plots the averaged power over all rotated line profiles and the intersecting half-power line.
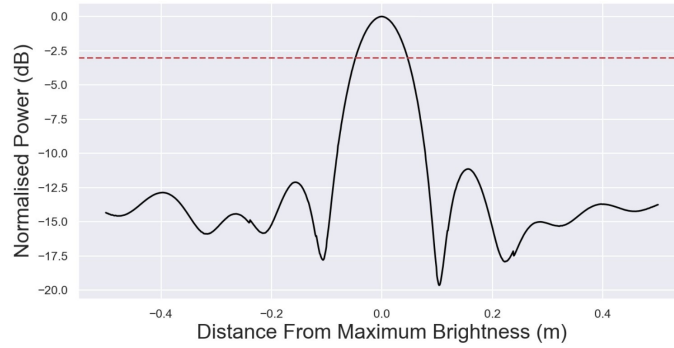

Figure 6: Plot of radially averaged power against the distance from brightest peak

The beam-width equals the distance between each intersection of the black plot and the dashed red line in Figure 6.

2.2.2 Directivity

The directivity D of a phased array antenna, measured in dB, is analogous to the signal to noise ratio (SNR) in the sense that the amount of radiation directed forwards represents the signal and the average intensity in all directions represents the noise. Although only an estimation, due to the restricted FOV, of the interference pattern I, D can be given by the following formula:

$$D(I) = 10 \cdot \log\left(\frac{\max(I)}{\text{mean}(I)}\right) \qquad (9)$$

Where $D(I)$ is the directivity in dB of the phased array and I is the interference pattern.

2.3 Phased Array Testing Methodologies

Working in a virtual, idealised environment provides numerous benefits; however, it also has certain limitations. In real-world situations, antenna positions might not match the intended design, electrical path lengths from the antenna to the data register could vary, and the phase centres of each sinuous antenna element may be inconsistent and depend on the direction of incoming radiation. Furthermore, various other unexpected factors not considered in a virtual setting often emerge during actual testing.

Researchers from the York Plasma Institute, who study the use of microwaves in fusion plasmas in collaboration with the Department of Engineering at the University of York, built an exact replica of the 9-antenna phased array used in the current SAMI-2 diagnostic. The purpose of this was to test the effect of adding foam behind the antennas in the hopes of reducing internal reflections and thus increasing data quality. This identical 'twin' array was set up for data collection in an anechoic chamber, facing a single emitting horn antenna. Time-series voltage measurements were collected from the diagnostic at a sampling frequency of *125 MHz*. Before detailing the data analysis methodology, it is worth briefly describing SAMI-2's composition.

2.3.1 SAMI-2 Diagnostic Overview

A number of dual-polarised sinuous antenna elements are arranged on the front face of a cylindrical, 3D-printed plastic frame. Directly behind each of these antennas, the two polarisation channels are fed into a printed circuit board (PCB) developed as part of Joe Allen's PhD thesis [6]. A detailed illustration of a PCB can be viewed below.
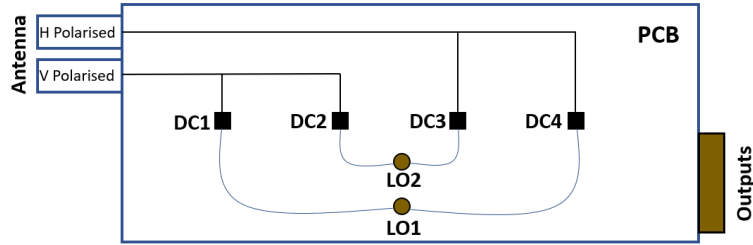

Figure 7: Diagram of a single PCB, showing which signals are inputs to which down-converter

The down-converters (DC), preserve the phase and amplitude information while shifting the signals in frequency space by an amount dictated by the local oscillator frequencies, LO1 and LO2. Each DC produces two components: the in-phase (*I*) and quadrature (*Q*) components representing a complex signal where $S_i = I_i + jQ_i$ for the ith antenna, where $j = \sqrt{-1}$. One reason why IQ mixers are used here, rather than standard down-converters, is their ability to retain both phase and amplitude information when converted to a complex signal. Retaining this phase information allows for the separation of the different side-bands, which is crucial for determining a frequency shift and therefore enabling the DBS capabilities of the diagnostic.

2.3.2 Signal Analysis

Part of the data analysis performed was ensuring the phase differences between each of the I and Q signals was $90°$. The power fed into each of the antennas was also checked because the LO power dividers did not evenly distribute the signals across the antennas. Additionally, each antenna's output power was compared when receiving both vertically and horizontally polarised light. The 9-antenna array recorded horizontally polarised light with twice the sensitivity of vertically polarised light, assuming both polarisations were incident at the same intensity.

2.3.3 Image Reconstruction

The power normalised complex signal, S_i recorded by the ith antenna is first Fourier transformed over a specified time interval Δt:

$$\hat{S}_i(\nu) = \int_0^{\Delta t} S_i(t)e^{2\pi j\nu t}\, dt \tag{10}$$

where $\hat{S}_i$ is the Fourier transform of S_i, ν is the frequency of the signal and $j = \sqrt{-1}$.

For each image pixel, p, the pixel specific complex phase factor, $e^{j\Phi_p(\bar{x})}$ is applied to $\hat{S}_i$ to shift its phase.

$$\hat{S}_p(\nu, \bar{x}) = \sum_{i=1}^{N} \hat{S}_i(\Delta\nu)e^{j\Phi_p(\bar{x})} \tag{11}$$

To find the intensity of the signal at that pixel, the square modulus of the signal is summed over $\Delta\nu$ in frequency space. To increase speed of computation, this is only applied to a narrow band of frequencies $\Delta\nu \approx \pm 0.2$ MHz around the frequency being imaged [6].

$$I_p(\nu, \bar{x}) = \int_{\Delta\nu} \left|\hat{S}_p(\nu, \bar{x})\right|^2 d\nu \tag{12}$$

where N is the number of antennas, $\bar{x}$ is the position vector from an antenna to a screen pixel

Ben Pritchard, a PhD student at the University of York, set up and performed experiments that allowed for the determination of true phase values for each direction $\Phi_p(\bar{x})$. The image creation method was tested using both real and synthetic data. The virtual data were generated as time-series, complex signals given a radially radiating point source placed at a known location. To construct an image with variable resolution from fixed grid calibration phases, the image is initially created at the calibration grid resolution and then interpolated to the desired level of detail.

3   Results

The following characters will be used throughout this report to represent different array designs .

Identifier	Description
(A)	20 Antennas Proposed
(B)	20 Antennas Random
(C)	9 Antennas (Current Array on SAMI-2)

Table 3: Identifier to Description Mapping

To demonstrate the effectiveness of the optimisation program, various properties of the optimised array can be compared to that of randomly generated arrays. The following figure shows how the gain varies both with the number of antenna elements and the number of optimisation iterations. It is important to make the distinction between the defnition of gain used in this report and what is commonly used in the literature. Gain in this report measures the ratio of main-lobe to side-lobe power whereas in the literature it is really just the directivity, as defined in section 2.2.2, that accounts for real world antenna losses.
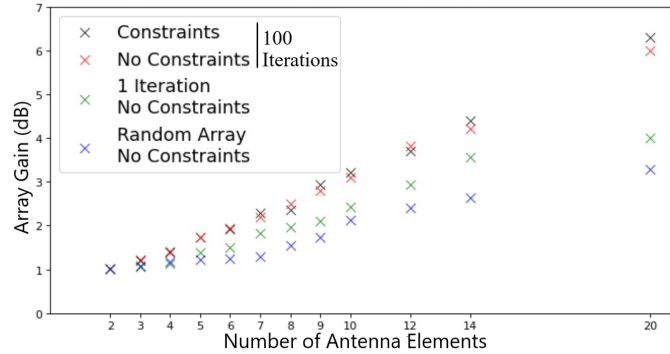

Figure 8: Plot of array gain against the number of antenna elements

It can be seen from Figure 8 that the gap in gain values between a randomly generated array and an optimised array grows with the number of antennas. This is because the space of all possible designs increases exponentially with the number of elements, thus the optimal design deviates increasingly from the random.

3.1   Properties of the Proposed Array

For both the 9-element and 20-element arrays, 2000 variants were generated by introducing random positional shifts of up to 1 *mm* to each antenna element. The property of interest was then calculated for each variant. To represent the property and its corresponding uncertainty, the mean and standard deviation were calculated. For comparison with the non-optimized 20-element array, the same process was carried out on 2000 randomly created arrays. The final quantitative results with their corresponding uncertainties can be found in Table 4. One might think of this particular approach to

calculating the uncertainties as a form of sensitivity analysis to the manufacturing errors in antenna placement.

Identifier	Angular Resolution ($°$)	Sidelobe Rejection (*dB*)	Directivity (*dB*)
(A)	(5.4 ± 0.1)	(-8.1 ± 0.2)	(13.4 ± 0.2)
(B)	(6.1 ± 0.5)	(-5.1 ± 0.9)	(12.2 ± 0.5)
(C)	(6.3 ± 0.3)	(-3.3 ± 0.2)	(9.8 ± 0.2)

Table 4: Table of angular resolution, sidelobe rejection, and directivity for different array designs

3.1.1 Angular Resolution

The angular resolution was found to be dependent on the pattern of the antennas. For instance, a 20-element array optimised using the uniformity of the distribution of baseline separations in x and y, yielded an angular resolution of $(4.9 \pm 0.1)°$, smaller than all other tested arrays. This came at the cost however, of higher powered sidelobes, which ultimately led to its rejection. An intentional side effect of the particular method chosen to score the array was that it did not just calculate the sidelobe rejection, it also penalised the design if the beam-width grew large enough to impinge on the cutoff circle. Therefore, *array-A* in Table 4, also has a reduced angular resolution.

3.1.2 Sidelobe Rejection vs Number of Antenna Elements

The sidelobe rejection value was found using the method outlined in section 2.1.3, for a varying number of antenna elements. The results of which are outlined in the following figure.
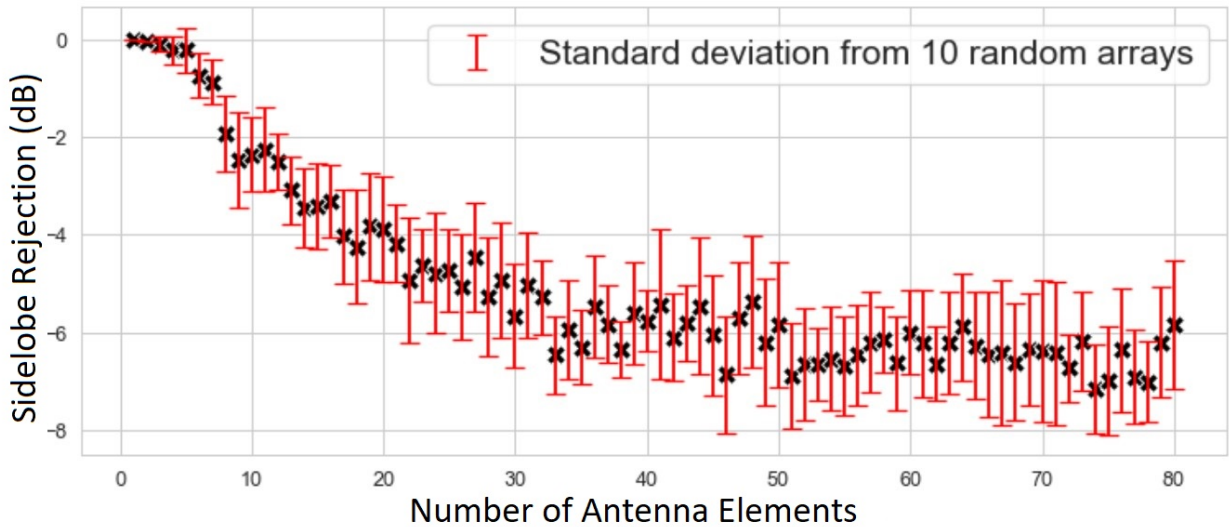

Figure 9: Sidelobe rejection values plotted against the number of antenna elements

It can be seen that the sidelobe rejection decreases rapidly with small numbers of antennas but begins to plateau after around *50* elements. One possible explanation for this is the method used to

calculate the sidelobe rejection relied on a maximum beam-width slightly greater than *20 cm*. Thus, if the central beam crossed that boundary, the algorithm may count it as a sidelobe rather than a central beam, misinforming the calculation for sidelobe rejection.

3.2 The Effect of Manufacturing Errors on Performance

The following is an illustration of the sensitivity in sidelobe rejection to manufacturing errors in the antenna placement, created using the same method as for the uncertainties.
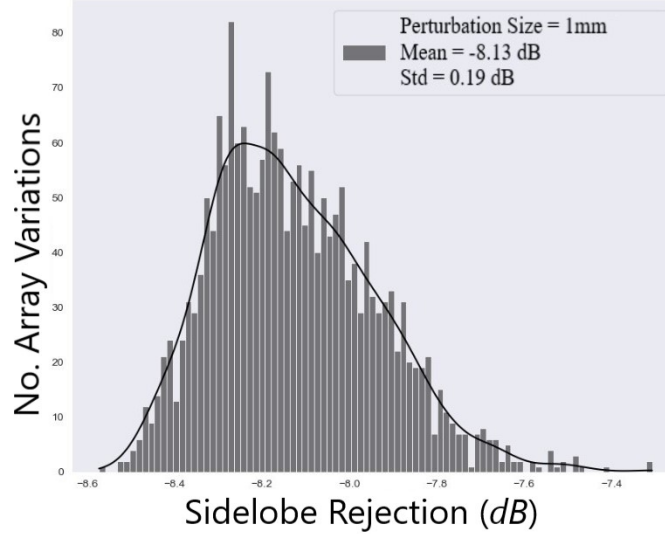

Figure 10: Histogram illustrating the distribution of sidelobe rejection values with a *1 mm* manufacturing tolerance.

As shown in Figure 10, even small variations in the positions of each antenna can cause large changes in the array's performance. With only 1 *mm* adjustments, the sidelobe rejection values range from -8.6 *dB* to -7.4 *dB*.

3.3 Image Reconstruction

In an idealised environment, each antenna image-pixel pair has a well-defined phase difference at a given frequency. One might expect that in reality, each antenna has an unknown yet constant phase centre and phase offset. If this were true, then a single set of measurements where a source was placed at a known location would be enough to calibrate the array. This is because each antenna would simply have a constant phase-offset which could be accounted for. However, it was found when applying this methodology that a coherent image was unobtainable. The phase-offset values were instead dependent on the direction of the source. Therefore, a grid of phase measurements had to be taken in order to calibrate the array. The following are images reconstructed using both calibrated, real data and idealised virtual data.
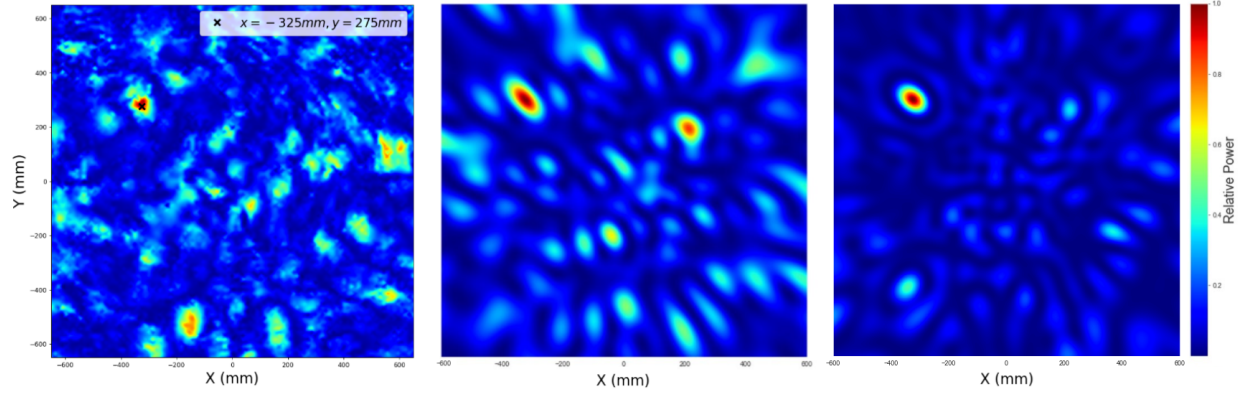
Figure 11: Image reconstructions of single source placed at $(-0.325, 0.275, 0.750)m$. Calibrated image from experimental data, taken with *array-C* (**left**), image from virtual data using *array-C* (**middle**) and image from virtual data using *array-A* (**right**)

As seen in Figure 11, although the virtual data was created with a point source and so should have zero width, the image reconstructed from experimental data had a smaller spot size. This could be due to the more directed radiation pattern of the sinuous antennas that simulated. To quantify the power of the most prominent sidelobe, a 2D peak search was conducted, and the average power within a $40\ mm$ radius of each peak was calculated. The results can be found in Table 5.

Identifier	Data Type	Max Sidelobe Power (dB)
(A)	Virtual	-5.1
(C)	Virtual	-2.0
(C)	Real	-2.4

Table 5: Table of Max Sidelobe Powers for Different Array Designs

It can be seen in Table 5 that the maximum sidelobe power is reasonably similar for both the experimentally collected and idealised data. This similarity suggests that the final performance of the proposed 20-element *array-(A)* will likely be comparable to the idealised results.

4   Discussion

Although further work could be done on improving image reconstruction, array calibration and data analysis, the core objectives of this project were accomplished. The successful creation of an optimised phased antenna array design for the SAMI-2 diagnostic was achieved along with various experiments testing performance physically and virtually. This design will be implemented into SAMI-2 and placed onto a diagnostic port window on the MAST-U spherical tokamak.

With respect to findings of the project, during image reconstruction attempts, it was found that each antenna not only had a unique phase error, that phase error depended on the direction of incident EM radiation. Therefore, to calibrate the array, a single source had to raster across a

2D grid while the phase at each antenna was measured. Another finding was that maximising the uniformity of the spread of antenna baselines does not necessarily result in minimising the sidelobe rejection as originally theorised. Furthermore, it has been stated that stochastic optimisation is not always a feasible approach when designing phased arrays due to its high computational demands [7] . Although more sophisticated optimization methods would have achieved a higher efficiency, the technique adopted here reached a steady state within a practical time period of hours not days.

An experiment that would have been beneficial to the generation of the interference pattern is the profiling of the sinuous antenna's radiation pattern. It was assumed that each antenna was isotropically sensitive, where in reality it may be more directed leading to different values for gain, directivity and beam-width. In terms of limitations of the array calibration procedure, phase measurements were only taken with a source along a 2D planar grid; the validity of this method needs to be assessed when the horn antenna varies in depth also. There are changes that could have been made during this project that would have improved the robustness of the final design. For one, only a single frequency, $20GHz$ was used in the creation of the interference pattern, when SAMI-2 operates from $(20 - 40)GHz$. In retrospect, a random frequency value should have been chosen for each pattern generation. The final objective function should have been a composite function representing all performance metrics outlined in Table 4.

One direction of future study in which this project could be taken is the application of neural networks to image prediction. Separate experiments were undertaken for this project that showed promise in the accurate prediction of radiation intensity images, just from antenna phase information. See Figure B.1 for an illustration of this. Another area of research that could prove fruitful would be developing a method of image artefact reduction using the predicted sidelobes in array interference patterns. Every beamformed direction has a different interference pattern: Interpreting these as sensitivity maps may allow for corrections to be applied to each pixel. This may not be feasible, but other similar ideas should be pursued.

5 Conclusion

The design of the phased array antenna layout was primarily limited by the physical constraints of the system. Given the size and shape of the system and its constituents, no more than *22* antennas could be placed without risk of component clashes. Although restricted in numbers, the positions of each antenna were successfully adjusted, to reach a final sidelobe rejection value of (-8.1 ± 0.2) *dB*, a significant improvement over non-optimised 20-element arrays which averaged (-5.1 ± 0.9) *dB*. This study has shown that stochastic optimisation using a beamforming derived objective function is suitable for use in designing aperiodic phased arrays. It has also been demonstrated, in Figure 11, that the use of a simulated virtual environment when predicting image properties is suitable to inform and guide design decisions. A key finding from this study is that it was not sufficient to maximise the number of unique baselines, if the goal was to minimise the sidelobe rejection value. Next steps for this research should include determining which image reconstruction method is most suitable to SAMI-2 and improving the calibration robustness.

References

[1] Braun, K. F. (1909). Electrical oscillations and wireless telegraphy. *Nobel Lecture*.

[2] R. L. Haupt and Y. Rahmat-Samii, (2015), Antenna Array Developments: A Perspective on the Past, Present and Future, *IEEE Antennas and Propagation Magazine*. vol. 57. pp. 86-96.

[3] A. Kharalkar, A. Batabyal, R. Zele and S. Gupta. A Review of Phased-Array Receiver Architectures for 5G Communications, (2022). *IEEE Region 10 Symposium (TENSYMP)*. pp. 1-6.

[4] Lockwood, G. R., Talman, J. R., & Brunke, S. S, (1998). Real-time 3-D ultrasound imaging using sparse synthetic aperture beamforming. *IEEE Transactions on Ultrasonics, Ferroelectrics, and Frequency Control*, vol. 45 no. 4, pp. 980-988.

[5] Thomas, D. A., Brunner, K. J., Freethy, S. J., Huang, B. K., Shevchenko, V. F., & Vann, R. G. L. (2016). 2D Doppler backscattering using synthetic aperture microwave imaging of MAST edge plasmas. *Nuclear Fusion*. vol. 56, no. 2.

[6] Allen, J. O. (2021). Design of the Synthetic Aperture Microwave Imager-2 for measurement of the edge current density on MAST-U. University of York, Department of Physics.

[7] P. Rocca, G. Oliveri, R. J. Mailloux and A. Massa, (2016), Unconventional Phased Array Architectures and Design Methodologies—A Review. *Proceedings of the IEEE*, vol. 104, no. 3, pp. 544-560.

[8] R. L. Haupt, (2007), Antenna Design With a Mixed Integer Genetic Algorithm, *IEEE Transactions on Antennas and Propagation*, vol. 55, no. 3, pp. 577-582.

[9] A. Massa, P. Rocca and G. Oliveri, Compressive Sensing in Electromagnetics - A Review, *IEEE Antennas and Propagation Magazine*, vol. 57, no. 1, pp. 224-238.

[10] C. S. Ruf, C. T. Swift, A. B. Tanner and D. M. Le Vine, (1988), Interferometric synthetic aperture microwave radiometry for the remote sensing of the Earth, *IEEE Transactions on Geoscience and Remote Sensing*, vol. 26, no. 5, pp. 597-611.

[11] A. B. Tanner and C. T. Swift, (1993), Calibration of a synthetic aperture radiometer, *IEEE Transactions on Geoscience and Remote Sensing*, vol. 31, no. 1, pp. 257-267.

[12] S. Kirkpatrick, C.D. Gelatt, M.P. Vecchi, Optimization by Simulated Annealing,(1987), *Readings in Computer Vision*, pp. 606-615.

[13] Robert Mailloux, (2017), *Phased Array Antenna Handbook*, Third Edition, Artech.

[14] S. J. Freethy, V. F. Shevchenko, & R. G. L. Vann, (2012), Optimization of Wide Field Interferometric Arrays via Simulated Annealing of a Beam Efficiency Function, *IEEE Transactions on Antennas and Propagation*, vol. 60, no. 11.

Acknowledgements

Appendices

Appendix A

During the investigation into virtual, single source image creation, one feature that was deemed difficult or perhaps impossible to predict was the depth at which that source was placed. So in order to study whether predicting the depth of a single source was possible or not, a simple neural network was built that takes the phase incident on each antenna as inputs and predicts the positions in polar coordinates of the source. The following regression plots demonstrate the performance of the neural network in predicting the direction from which an emitting source is placed.
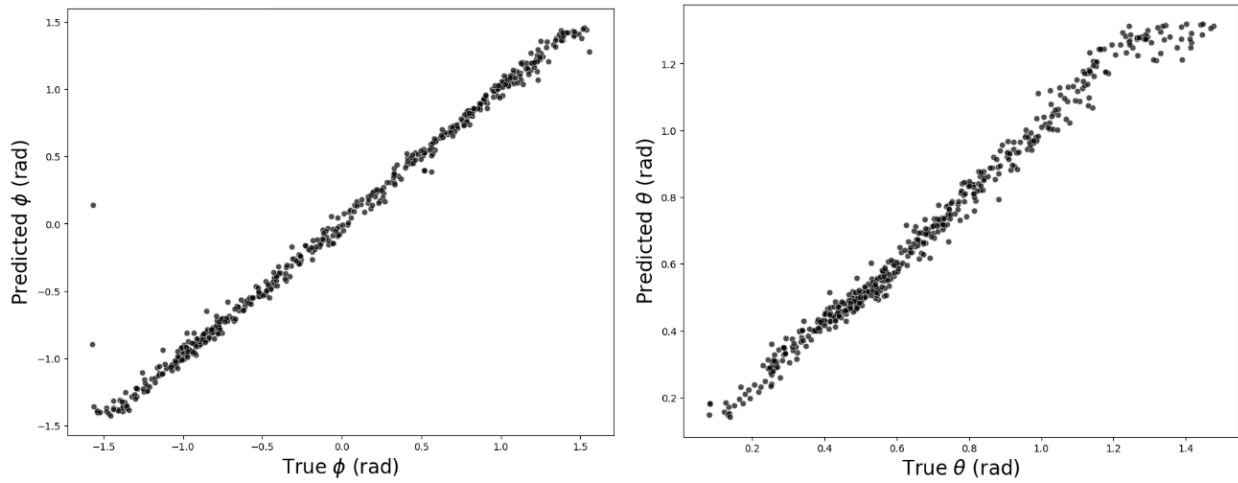

Figure A.1: Plots regressing predicted against true source directions (θ and ϕ)

As shown in Figure A.1, the model predicts the direction of the signal source accurately until θ or ϕ approaches 0 or 2π. However, the depth of the source proved more difficult to predict. After many more training iterations and a change in model architecture, the below performance was achieved.
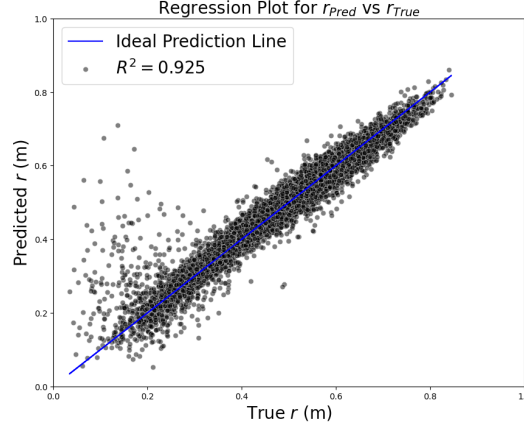
Figure A.2: Regression plot that compares the predicted source depth with the true source depth. The blue line shows perfect predictions

An R^2 value of 0.93 shows that a high degree of the variance in source depth was predicted by the model. An interesting limitation of this model seems to be its inability to accurately predict source depth in the near field ($r < 0.2m$).

This sub-study demonstrates the possibility of predicting depth and direction of a single source in 3D space, however, there are some major limitations that need to be considered. To create a whole 2D image, more than just single source location prediction is necessary. In reality, the measured phases vary widely from what is expected as discussed in section 3.5. This variation in phase may be larger than the maximum allowed in order to predict the direction and depth of a source with accuracy.

Appendix B

This technique would have to be tested further by adding noise in the frequency domain and in order to be useful and applicable to SAMI-2. A slightly more advanced model architecture with CNN (convolutional neural network) layers to process spatial data was built to output entire images based only on the input of single phase values for each antenna. The following images were outputted from a model trained on 10,000 random images generated from Perlin noise. The phases at each antenna were determined by assuming a single frequency with the antenna positions specified by *array-(C)*. Intensity was represented by each pixel in the image, so the square root of each pixel represented the radiation's initial amplitude. Complex signals were then generated for each antenna and were summed across all pixels. A Fourier transformation was performed on these summed signals, the phase could then be extracted for each antenna.These single phase values were the only inputs to the model.
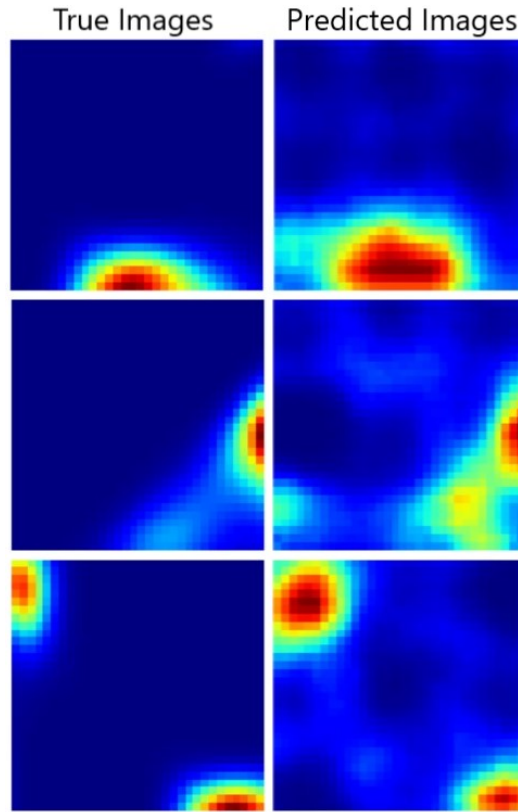
Figure B.1: Plots of three unseen microwave radiation patterns (***left***) vs corresponding predicted images (***right***)

This process will need to be greatly improved and rigorously tested if it is to find application in fusion plasma imaging. A model would need to be trained or fine tuned on experimentally collected data and set up image multiple frequencies. The final image quality should then be assessed against previous methods and its benefits and pitfalls found.